

# MID-INFRARED COLORS OF DWARF GALAXIES: YOUNG STARBURSTS MIMICKING ACTIVE GALACTIC NUCLEI

KEVIN N. HAINLINE

Steward Observatory, University of Arizona, 933 North Cherry Avenue, Tucson, AZ 85721, USA

AMY E. REINES<sup>1</sup>

National Optical Astronomy Observatory, Tucson, AZ 85726, USA

JENNY E. GREENE

Department Astrophysical Sciences, Princeton University, Princeton, NJ 08544

DANIEL STERN

Jet Propulsion Laboratory, California Institute of Technology, 4800 Oak Grove Drive, Mail Stop 169-221, Pasadena, CA 91109, USA

Received 06/23/16; accepted 09/20/16

## ABSTRACT

Searching for active galactic nuclei (AGN) in dwarf galaxies is important for our understanding of the seed black holes that formed in the early Universe. Here, we test infrared selection methods for AGN activity at low galaxy masses. Our parent sample consists of 18,000 nearby dwarf galaxies ( $M_* < 3 \times 10^9 M_\odot$ ,  $z < 0.055$ ) in the Sloan Digital Sky Survey with significant detections in the first three bands of the AllWISE data release from the Wide-field Infrared Survey Explorer (*WISE*). First, we demonstrate that the majority of optically-selected AGNs in dwarf galaxies are not selected as AGNs using *WISE* infrared color diagnostics and that the infrared emission is dominated by the host galaxies. We then investigate the infrared properties of optically-selected star-forming dwarf galaxies, finding that the galaxies with the reddest infrared colors are the most compact, with blue optical colors, young stellar ages and large specific star formation rates. These results indicate that great care must be taken when selecting AGNs in dwarf galaxies using infrared colors, as star-forming dwarf galaxies are capable of heating dust in such a way that mimics the infrared colors of more luminous AGNs. In particular, a simple W1 – W2 color cut alone should not be used to select AGNs in dwarf galaxies. With these complications in mind, we present a sample of 41 dwarf galaxies worthy of follow-up observations that fall in *WISE* infrared color space typically occupied by more luminous AGNs.

*Subject headings:* cosmology: observations – galaxies: evolution – galaxies: dwarf galaxies – galaxies: active galactic nuclei

## 1. INTRODUCTION

There is now an overwhelming body of evidence suggesting that all massive galaxies host a central supermassive black hole which grows alongside the stellar population (Kormendy & Richstone 1995; Kormendy & Ho 2013). In addition, a relationship has been observed between the central black hole mass and the galaxy bulge stellar velocity dispersion that spans many orders of magnitude (Gebhardt et al. 2000; Ferrarese & Merritt 2000). The origin of this relationship is still not well understood, but current theories imply that galaxy mergers and interactions play a role, both in increasing the stellar mass of a galaxy and in driving gas towards the centers of galaxies, feeding black holes (Hopkins et al. 2008; Koss et al. 2010; Ellison et al. 2011; Bessiere et al. 2012; Sabater et al. 2013). However, this view of galaxy growth implies the existence of low mass “seed” black holes that must have existed at high redshift. To understand these difficult-to-observe objects, researchers have turned to observations of nearby dwarf galaxies which may host analogous

lower-mass black holes (for a review, see Reines & Comastri 2016, submitted). By assembling large samples of low-mass black holes, it may be possible to distinguish between the different proposed theoretical scenarios for their creation: these objects may be remnants of massive Population III stars (Bromm & Yoshida 2011), a result of direct collapse of primordial dense gas (Haehnelt & Rees 1993; Lodato & Natarajan 2006; Begelman et al. 2006; van Wassenhove et al. 2010), or perhaps they are the end product of very massive stars formed through stellar mergers in dense star clusters (Gürkan et al. 2004; Freitag et al. 2006; Goswami et al. 2012; Giersz et al. 2015; Lützgendorf et al. 2016).

Assembling these large samples of low-mass black holes is made difficult by the fact that resolving their gravitational sphere of influence is currently not feasible at distances larger than a few Mpc. However, active galactic nuclei (AGN) emission across the electromagnetic spectrum can be used to infer the existence of a black hole. Observations at optical wavelengths have been used to uncover AGNs in NGC 4395 (Filippenko & Sargent 1989; Filippenko & Ho 2003) and POX 52 (Barth et al. 2004),

<sup>1</sup> Hubble Fellow

while data at X-ray and radio wavelengths have been used to find AGNs in both Henize 2-10 (Reines et al. 2011; Reines & Deller 2012) and the dwarf galaxy pair Mrk 709 (Reines et al. 2014). Larger samples of low-mass AGNs have been uncovered at optical (Greene & Ho 2004, 2007; Dong et al. 2012; Reines et al. 2013; Moran et al. 2014) and X-ray (Lemons et al. 2015; Mezcua et al. 2015; Pardo et al. 2016) wavelengths, which have been targeted with successful follow-up observations (Baldassare et al. 2016), including the discovery of a  $5 \times 10^4 M_{\odot}$  BH in RGG 118 (Baldassare et al. 2015).

One important and often-used method for selecting luminous AGNs relies on observations made in the mid-IR, where dust, heated by the central accreting black hole, reprocesses the light and emits with a characteristic red IR power-law spectrum. Infrared emission only minimally suffers from nuclear and galaxy-scale obscuration, and so mid-IR observations have successfully uncovered large numbers of unobscured and obscured luminous AGNs and quasars (Lacy et al. 2004, 2013; Stern et al. 2005; Hickox et al. 2007; Donley et al. 2008; Ashby et al. 2009; Assef et al. 2010; Stern et al. 2012; Mendez et al. 2013; Hainline et al. 2014). The all-sky mid-IR coverage of the *Wide-field Infrared Survey Explorer* (*WISE*, Wright et al. 2010) has allowed for observations of large samples of objects, and multiple authors have proposed *WISE* color schemes which select for the red AGN power law emission in the infrared (Jarrett et al. 2011; Stern et al. 2012; Mateos et al. 2012). These selection methods rely on the fact that AGNs are capable of heating dust to temperatures well above what is observed from stellar processes in moderate to high-mass galaxies, and have demonstrated high levels of reliability when applied to these objects.

Recently, Satyapal et al. (2014) and Sartori et al. (2015) used mid-IR selection methods to assemble large samples of low-mass galaxy AGN candidates from *WISE* data. Under the assumption that *WISE* selection targets optically obscured, “hidden” AGNs in these objects, these authors draw broad conclusions about the population of low-mass black holes. The Satyapal et al. (2014) study targets “bulgeless” galaxies without optical evidence for an AGN, and the authors conclude that star formation is not the primary source of the IR emission in their sample. In addition, they propose that the fraction of galaxies hosting IR-selected AGN activity *increases* at low masses. This puzzling trend was also seen (with lower significance) using a larger sample of dwarf galaxies by Sartori et al. (2015), who compared multiple AGN selection methods and concluded that dwarf galaxies with *WISE* colors indicative of AGN activity are bluer and potentially may have more ongoing star formation and lower metallicities than those selected using optical emission lines.

These results are intriguing in light of the fact that no other tracer of AGN activity has thus far uncovered such large samples of AGNs in dwarf galaxies. In most AGN selection regimes, more luminous AGNs are easier to find both because massive BHs have a higher Eddington limit and because of increasing confusion due to star formation at low mass. Thus, the observed increase in AGN fraction at the lowest dwarf galaxy masses is puzzling. Low-mass SMBHs that exist in dwarf galaxies

power AGNs that have such low luminosities that star formation in their hosts becomes a significant source of contamination. In particular, it has been shown that low-metallicity dwarf starburst galaxies are capable of heating dust to very high temperatures (Hirashita & Hunt 2004; Reines et al. 2008; Izotov et al. 2011, 2014; Griffith et al. 2011; Rémy-Ruyer et al. 2015), producing red mid-IR colors. This was recently explored in O’Connor et al. (2016), who found that galaxies with low stellar masses have predominantly red *WISE* colors, which the authors associate with higher specific star formation rates (sSFR) in these galaxies. Thus, it may be that using common mid-IR AGN selection methods on dwarf galaxies results in the selection of a large number of star-forming galaxies that contaminate the samples, leading to erroneous conclusions about AGN fractions at these masses.

In this paper, we use *WISE* data to empirically examine the infrared colors of dwarf galaxies as a function of their properties as probed by Sloan Digital Sky Survey (SDSS) data. Our results suggest that star formation, and not AGN activity, is responsible for the red *WISE* colors for the majority of the dwarf galaxy population (also see Izotov et al. 2014). We propose a small sample of dwarf galaxy AGN candidates that require follow-up observations to confirm black hole activity.

In Section 2, we discuss our sample selection, and describe how these objects were matched to *WISE* photometry. We start by exploring the infrared properties of dwarf galaxies which have optical spectroscopic evidence for an AGN in Section 3.1. We then investigate optically-selected star-forming galaxies and propose a sample of IR-selected AGN candidates in Section 3.2. We expand our sample to include IR-selected AGN candidates without optical emission line flux measurements Section 3.3, after which we compare these objects to samples of IR-selected AGN candidates presented in the literature in Section 3.4. Finally, we explore our *WISE* detection limits in Section 3.5 and we discuss our results and draw conclusions in Section 4.

## 2. SAMPLE SELECTION AND DATA

The dwarf galaxies we explore in this paper were selected from the NASA Sloan Atlas (NSA), a catalogue of galaxies at  $z < 0.055$  selected from the Sloan Digital Sky Survey (SDSS) DR8 (York et al. 2000; Aihara et al. 2011), where the observations were re-analyzed, resulting in improved photometry (Blanton et al. 2011), and spectroscopy (Yan 2011; Yan & Blanton 2012). In addition, stellar-masses for each object were derived with the `kcorrect` code of Blanton & Roweis (2007), which uses the stellar population synthesis models of Bruzual & Charlot (2003) and the nebular emission-line models of Kewley et al. (2001). These masses are provided in the NSA in units of  $M_{\odot} h^{-2}$ , and in this paper we have assumed  $h = 0.73$ .

Following Reines et al. (2013), we selected all galaxies with  $M_{*} < 3 \times 10^9 M_{\odot}$ , the approximate mass of the Large Magellanic Cloud (van der Marel et al. 2002). We matched those objects to the AllWISE data release (Cutri & et al. 2013), which provides increased sensitivity as compared to the previous *WISE* All-Sky data release. We note that because of the polar orbit of the *WISE* telescope, the total exposure time across the full sky is non-uniform and depends on both the sky position

and the zodiacal foreground emission. As  $W1 - W2$  color forms the basis for both of the primary AGN selection criteria that we will explore in this study (that of Jarrett et al. 2011; Stern et al. 2012), and given the importance of deep data at  $\lambda < 5\mu\text{m}$  for separating emission from dust heated by star formation and AGN activity, we chose to use the updated AllWISE data, with  $W1$  ( $3.4\mu\text{m}$ ) and  $W2$  ( $4.6\mu\text{m}$ )  $5\sigma$  sensitivities of  $54\mu\text{Jy}$  and  $71\mu\text{Jy}$ , respectively (compared to  $68\mu\text{Jy}$  and  $111\mu\text{Jy}$  in the All-Sky data release). These sensitivities are the minimum depth of the survey estimated for low coverage sky away from the Galactic plane.

When cross-matching with the AllWISE catalogue, we used a  $5''$  matching radius, and then chose the specific *WISE* photometry for each object based on the *WISE* ext\_flg value. Following the AllWISE Explanatory Supplement<sup>2</sup>, for most objects (ext\_flg= 0 or 4), we chose the “profile-fitting” photometric magnitudes, which are optimized for objects which are unresolved in *WISE*. For those objects where ext\_flg= 1,2, or 3, we used the “standard” aperture magnitudes, which better traces the photometry for objects that are resolved. Finally, for a small subset of objects with 2MASS photometry, where ext\_flg= 5, we used the photometry using apertures scaled from the 2MASS XSC shape values. Each object was only included in our sample if the signal-to-noise ratio (SNR) for the  $W1$ -,  $W2$ -, and  $W3$ -band photometry was greater than 3, yielding a sample of 18,482 dwarf galaxies with significant *WISE* detections. The majority of the objects were removed from our final sample because of their low SNR  $W3$  photometry ( $\sim 58\%$  of the total NSA sample, compared to  $\sim 4\%$  and  $\sim 7\%$  for  $W1$  and  $W2$ , respectively). The median  $W1 - W2$  and  $W2 - W3$  color uncertainties are 0.07 and 0.19, respectively, which we show with error bars in our *WISE* color-color diagrams.

While we have attempted to account for resolution effects with our usage of the *WISE* ext\_flg value to choose appropriate photometry for each object, we also wish to highlight some systematic effects that could affect our results. First, the  $W1$ ,  $W2$ , and  $W3$  bands have angular resolutions of  $6''.1$ ,  $6''.4$ , and  $6''.5$ , respectively (Wright et al. 2010). As a result, for any object that is slightly resolved in  $W1$  but not in  $W2$ , the resulting  $W1$  flux would be underestimated, resulting in a redder  $W1 - W2$  color. This effect could potentially move objects into the *WISE* color space spanned by AGNs. In addition, for objects with existing 2MASS photometry, which are largely well-resolved by *WISE*, colors estimated using apertures scaled from the 2MASS XSC shape value might be artificially blue as these apertures may contain foreground stars. Furthermore, these apertures may not contain all of the infrared emission from the object, leading to a systematic underprediction of the fluxes (see Cluver et al. 2014, for an examination of this effect). Because of these photometric effects, we have carefully visually examined the objects that have red *WISE* colors indicative of potential AGN activity, although objects with ext\_flg= 5 represent a small percentage of the total sample.

### 3. MID-IR PROPERTIES OF DWARF GALAXIES AND AGN CANDIDATES

<sup>2</sup> <http://wise2.ipac.caltech.edu/docs/release/allwise/expsup/>

#### 3.1. Optically-Selected AGNs and Composite Galaxies

We begin our analysis of the IR properties of dwarf galaxies by exploring the IR colors of the AGNs and composite dwarf galaxies selected from Reines et al. (2013). These 136 dwarf galaxies were initially chosen from their optical spectroscopic properties and specifically their position on the BPT diagram (Baldwin et al. 1981), a common optical emission-line diagnostic diagram that plots the flux ratio of  $[\text{OIII}]\lambda 5007/\text{H}\beta$  against  $[\text{NII}]\lambda 6583/\text{H}\alpha^3$ . This diagram separates AGNs from star-forming galaxies based on commonly-used dividing lines, an empirical line given in Kauffmann et al. (2003), and a theoretical “maximum starburst line” from Kewley et al. (2001). Objects above the Kewley et al. (2001) maximum starburst line on the diagram are often categorized as AGNs, while objects between the Kauffmann et al. (2003) and Kewley et al. (2001) lines are thought to have contributions to their emission line flux from both star formation and AGN activity, and are known as “composite” objects.

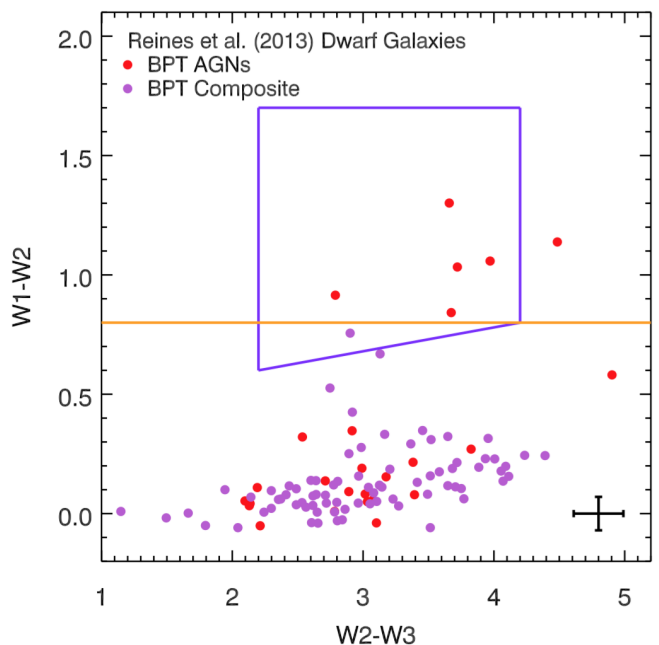


FIG. 1.— *WISE* color-color diagram for the dwarf galaxies from Reines et al. (2013) selected as AGN (red points) or composite galaxies (purple points) by their position on the BPT diagram. Four galaxies from the full Reines et al. sample did not have a match to the AllWISE catalogue, and 28 galaxies do not have significant detections in the  $W1$ ,  $W2$  or  $W3$  bands, as required to place them on this plot. We plot two common AGN selection criteria with different colored lines. In blue, we plot the selection box from Jarrett et al. (2011), and in orange, we plot the  $W1 - W2 > 0.8$  color criteria from Stern et al. (2012). We also plot the median  $W1 - W2$  and  $W2 - W3$  uncertainties with the error bars in the bottom-right corner.

Of the 136 BPT AGNs and composites from Reines et al. (2013), 104 objects have significant *WISE* detections as described in Section 2 (four objects did not have a match to the AllWISE catalogue, and the other 28 ob-

<sup>3</sup> Reines et al. (2013) also identified a sample of AGNs with broad  $\text{H}\alpha$  emission as potential AGN candidates, but in this section we focus only on those objects in their sample with optical emission line ratios indicative of AGN activity.

jects do not have significant detections in the W1, W2 or W3 bands). We plot these 104 dwarf galaxies on the infrared AGN diagnostic *WISE* color-color plot in Figure 1, which compares the W1 – W2 color to the W2 – W3 color. We color the points based on whether they were classified as an optical AGN (red) or composite galaxy (purple). We also plot common infrared AGN selection criteria with colored lines. In blue, we plot the selection box from Jarrett et al. (2011), and in orange, we plot the W1 – W2 > 0.8 color criteria from Stern et al. (2012). These selection boxes select for luminous quasars by the presence of power-law emission that extends from the W1 through W3 bands due to reprocessed emission from the dust torus from around the accretion disk feeding the central supermassive black hole. As can be seen from Figure 1, the majority of the dwarf galaxies selected as AGNs and composite objects by their optical emission would *not* be selected as IR AGN on this diagram. Only six of the Reines et al. (2013) BPT-AGN dwarf galaxies would be selected as AGN by the Stern et al. (2012) criterion. Five BPT-AGN and one BPT-composite object would be selected as an AGN by the Jarrett et al. (2011) criteria. We plot the SDSS and *WISE* thumbnail images for these six objects in Figure 2. From this Figure, it can be seen that these optically-selected AGNs have significant *WISE* detections out to the longest wavelengths probed by *WISE*, evidence of an underlying infrared power-law from AGN-heated dust. As discussed in the introduction, more luminous AGNs are more likely to be found with *WISE* selection, as their infrared emission can be observed above the emission from dust heated by host galaxy star formation. This helps to explain the general trends observed in Figure 1, where five out of six of the objects in the Jarrett et al. (2011) selection box are BPT-AGNs.

The majority of both the BPT-AGNs and BPT-composite dwarf galaxies lie below the AGN selection regions in the area occupied by star-forming galaxies. These objects form a sequence that moves from blue W1 – W2 and W2 – W3 colors to the right and towards redder W2 – W3 colors. For these objects, the AGN IR luminosity must be low enough that the reprocessed infrared emission is overwhelmed by the emission from both the galaxy’s stellar continuum, the continuum emission from dust heated by star formation throughout host galaxy, and polycyclic aromatic hydrocarbon (PAH) emission. We will explore this in more detail in the next section.

### 3.2. *Optically-Selected Star-Forming Dwarf Galaxies*

We now look at the dwarf galaxies in the NSA with line ratios dominated by star formation. We use a subsample (N = 14,013) of our *WISE*-selected dwarf galaxies that have significant (SNR > 3.0) SDSS detections of the strong optical emission lines (H $\beta$ , [OIII] $\lambda$ 5007, H $\alpha$  and [NII] $\lambda$ 6583) and fall in the star-forming part of the BPT diagram. We use the wealth of SDSS optical data to understand how dwarf galaxy SF properties relate to *WISE* infrared colors and explore the potential origin of the red *WISE* colors observed in some dwarf galaxies. In Figure 3, we show the star-forming subsample on the BPT diagram with points colored by W1 – W2 infrared color. We plot those dwarf galaxies with W1 – W2 > 0.8, the selection criteria used to select AGNs from Stern et al.

(2012), using black stars. For these star-forming dwarf galaxies, we can see that, generally, the W1 – W2 color becomes redder as you move upwards and to the left on the sequence. Star-forming galaxies on the BPT diagram form a sequence in metallicity. Objects with the reddest *WISE* colors are among the lowest metallicity galaxies in our sample and also have the largest ionization parameters (see Kewley et al. 2013, for a review of how objects move on the star-forming region of the BPT diagram).

#### 3.2.1. *Physical Properties of Star-Forming Dwarf Galaxies*

We can use the SDSS spectroscopic data to derive properties of the stellar populations in the dwarf galaxies for comparison to their *WISE* colors. Some properties, such as galaxy size and optical color, are taken directly from the NSA, but in this section, we outline the methods we use to estimate the host galaxy star formation rate (SFR), stellar age, and ionizing luminosity.

*Star Formation Rates.* The luminosity of H $\alpha$  can be used to measure the star formation rate for a galaxy, following Kennicutt & Evans (2012):

$$\log(SFR[M_{\odot} \text{ year}^{-1}]) = \log(L(\text{H}\alpha) [\text{erg s}^{-1}]) - 41.27 \quad (1)$$

We have corrected the H $\alpha$  luminosity for the effects of extinction, using an intrinsic Balmer ratio of  $F_{\text{H}\alpha}/F_{\text{H}\beta} = 2.86$ ,  $R_V = 3.1$  and the O’Donnell (1994) extinction curve. This method of estimating extinction is more valid in regions of low obscuration, and is not reliable for the most obscured regions. We also calculate the specific star formation rates (sSFR), the star formation rate divided by the stellar mass of a galaxy. Since the H $\alpha$  emission line fluxes were measured using 3" diameter fibers<sup>4</sup>, we calculated the sSFR for each galaxy using masses estimated from the *fiberflux* values given in the NSA. These fluxes, which were measured within a 3" aperture, were converted to a stellar mass using the method discussed in Reines & Volonteri (2015), where we used the color-dependent mass-to-light ratio from Zibetti et al. (2009), adopting a solar absolute *i*-band magnitude of 4.56 mag (Bell et al. 2003). While most of the sources have sSFR < 1.0 Gyr<sup>-1</sup>, the majority of the red *WISE* sources have sSFR > 1.3 Gyr<sup>-1</sup>. In addition, we also use the Petrosian half-light radius from the NSA to estimate the SFR surface density ( $\Sigma_{\text{SFR}}$ ), the SFR divided by the area of the galaxy in kpc<sup>2</sup>.

*Stellar Age.* The EW of the hydrogen Balmer lines anticorrelates with the age of a stellar population (Stasińska & Leitherer 1996). We estimate stellar ages by comparing measured H $\alpha$  values to STARBURST 99 models (Leitherer et al. 1999), assuming a Salpeter (1955) IMF with power-law  $\alpha = 2.35$ , and a metallicity of  $Z = 0.004$  (where  $Z = 0.02$  represents solar metallicity). The majority of the galaxies with red *WISE* colors have high H $\alpha$  EWs and inferred stellar ages less than 7 Myr.

*Ionizing Luminosity.* We use the extinction-corrected H $\alpha$  luminosity to estimate the rate of ionizing photons

<sup>4</sup> The H $\alpha$  flux and EW estimates we use in this work are measured from SDSS fiber measurements and are dependent on the exact morphology and redshifts of the galaxies. As a result, we may be missing H $\alpha$  flux from star formation outside the fiber aperture. The majority of those objects with red *WISE* colors are smaller than the SDSS aperture.

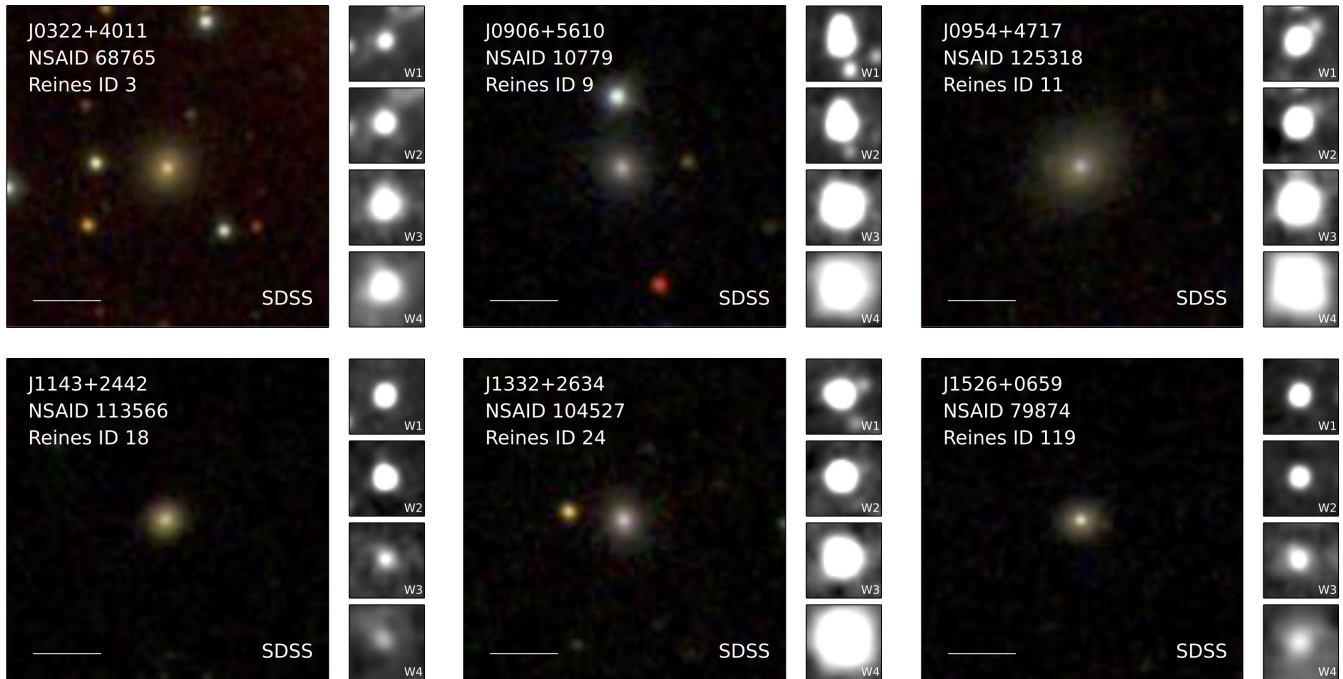


FIG. 2.— SDSS and *WISE* thumbnails for the Jarrett et al. (2011) *WISE* AGN candidates in the BPT AGN and composite region of the BPT diagram (Reines et al. 2013). Each object is labelled with both the NSAID (see Table 1) as well as the ID from Reines et al. (2013) in the SDSS image. The SDSS multi-band image is on the left, and on the right, the *WISE* W1, W2, W3, and W4 images are shown from top to bottom. In each panel, north is up, and east is to the left, and the bar in the bottom left of each SDSS panel is  $10''$  in length. Both the SDSS and *WISE* thumbnails are  $48''$  on a side. At the median redshift of our sample,  $z = 0.03$ ,  $1'' = 0.6$  kpc.

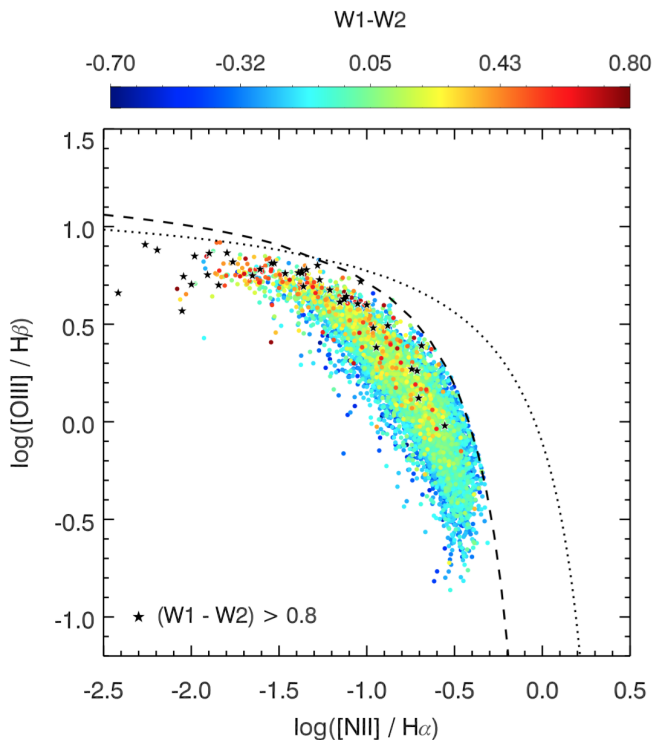


FIG. 3.— BPT ionization diagram for the star-forming dwarf galaxies described in Section 3.2. The points are colored by their  $W1-W2$  infrared color, and those objects with  $W1-W2 > 0.8$ , the criteria used in Stern et al. (2012) for selecting AGN candidates, are plotted with black stars. Overall, there is an observed trend in the figure between position to the top left of the star-forming sequence and red *WISE*  $W1-W2$  color.

( $Q_{\text{Lyc}}$ ) for these objects following the procedure from Reines et al. (2008):

$$\left(\frac{Q_{\text{Lyc}}}{\text{s}^{-1}}\right) \geq 2.25 \times 10^{12} \left(\frac{T_e}{10^4 \text{K}}\right)^{0.07} \left(\frac{L_{\text{H}\alpha}/2.86}{\text{erg s}^{-1}}\right) \quad (2)$$

Here, we start from Equations (2) and (3) from Condon (1992), and then assume Case B recombination, where  $F_{\text{H}\alpha}/F_{\text{H}\beta} = 2.86$ . We further assume an electron temperature of 10,000 K (Izotov et al. 1997), and, as seen from the above equation, our estimated ionizing photon rate is only a lower limit due to the fraction of ionizing radiation that is absorbed by dust or escapes the star-forming regions before ionizing hydrogen atoms. The dwarf galaxies in our sample with the reddest  $W1-W2$  colors have large  $\text{H}\alpha$  luminosities and values of  $Q_{\text{Lyc}}$  equivalent to greater than several thousand O-type stars.

### 3.2.2. Mid-IR Colors of Star-Forming Dwarf Galaxies

To investigate the origin of the infrared emission from the star-forming dwarfs, we plot the optical  $g-r$  and infrared  $W1-W2$  colors for these objects in Figure 4. Here, we can see that the galaxies with the *bluest* optical colors have the *reddest* infrared colors. We have colored the points by the equivalent width (EW) of the  $\text{H}\alpha$  emission line taken from the NSA, and we see that those dwarf galaxies with the reddest *WISE* colors have the highest  $\text{H}\alpha$  EW. We plot *WISE*  $W1-W2$  color as a function of  $\Sigma_{\text{SFR}}$  for each galaxy in Figure 5, and we see that the majority of the objects with the reddest  $W1-W2$  colors also have the highest  $\Sigma_{\text{SFR}}$ , further supporting the idea that we are observing compact young starbursts in these dwarf galaxies with red *WISE* colors. We note that

our usage of aperture fluxes to derive SFRs would lead to values of  $\Sigma_{\text{SFR}}$  for objects with Petrosian half-light radii larger than the SDSS fiber to be underestimated, although this effect does not significantly change the results seen in Figure 5.

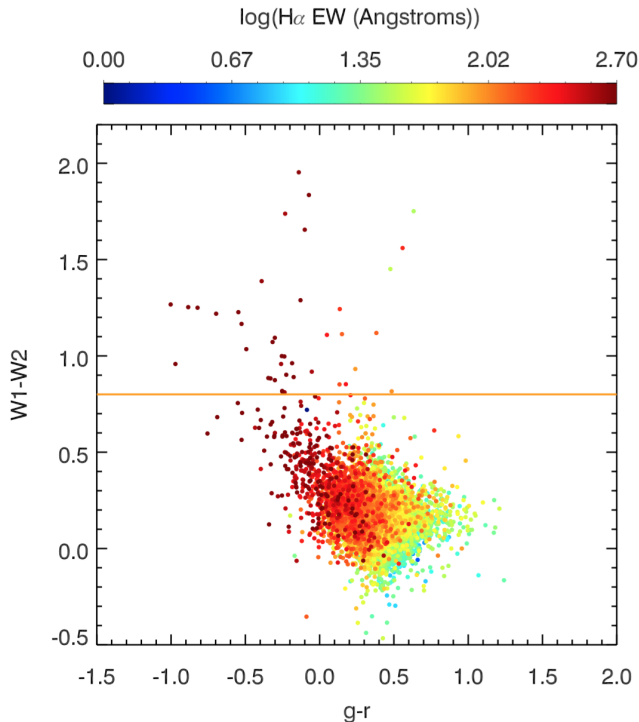


FIG. 4.— Optical to infrared color for the dwarf galaxies described in Section 3.2. The host galaxies with the reddest *WISE* colors are, on average, more optically blue, with the highest H $\alpha$  EWs and youngest ages.

We show *WISE* color-color diagrams for the dwarf star-forming galaxies in Figure 6. We color the points based on the EW (left panel) and luminosity (right panel) of the H $\alpha$  emission line. In both panels of Figure 6, we also plot the same AGN selection boxes shown in Figure 1. We can see that the majority of the objects lie outside the Jarrett et al. (2011) selection box. At the reddest W2 – W3 colors, the star-forming sequence extends upwards to redder W1 – W2 colors, wrapping around the Jarrett et al. (2011) AGN selection box and above the Stern et al. (2012) selection line. In the left panel of Figure 6, we see that those objects with the reddest *WISE* infrared colors have the largest H $\alpha$  EW values and youngest stellar ages, also indicated in Figure 4. Similarly, in the right panel of Figure 6, we can see an even stronger trend for the objects with the reddest *WISE* colors to have the largest H $\alpha$  luminosities, and rate of ionizing photons.

We explore the dwarf galaxy sequence on the *WISE* color-color diagram as a function of dust temperature in Figure 7. Here, on the left, we plot the same dwarf galaxies and AGN selection boxes as in Figure 6, but now the objects are colored by their specific star formation rates (sSFR). We see that the sequence of BPT-selected star-forming dwarf galaxies drives to the right and upward, and is correlated with the sSFR. We also plot extreme *WISE* dwarf galaxies from Griffith et al. (2011) and Izotov et al. (2011), which have W1 – W2  $\sim$  2.0. These rare

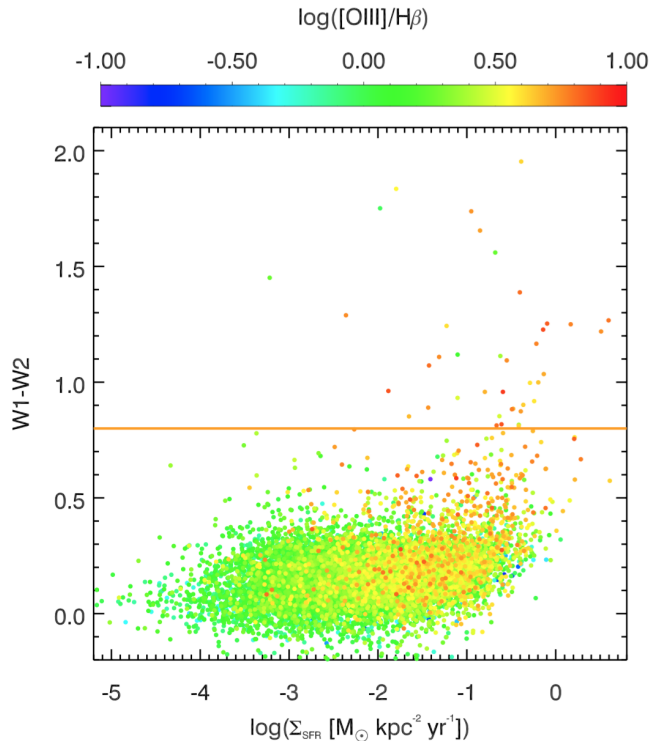


FIG. 5.— *WISE* W1 – W2 color plotted against the SFR surface density ( $\Sigma_{\text{SFR}}$ ) for the dwarf galaxies described in Section 3.2, with the points colored by [OIII]/H $\beta$  line ratio. Those galaxies with the reddest W1 – W2 colors have the highest SFR surface densities.

objects are at the extreme end of the sequence traced by the star-forming dwarf galaxies in our sample. We also plot the *WISE* colors for the infrared-bright star-forming galaxies Arp220 and M82, as measured from their SWIRE SED templates (Polletta et al. 2007). Finally, in this panel we plot color tracks that we generated by linearly combining an elliptical galaxy template from Assef et al. (2010) with a simple single-temperature blackbody (BB) at  $z = 0$ . For these tracks, we chose an elliptical galaxy template as this template does not show evidence for dust in the infrared. We plot three tracks at three different dust temperatures: 400 K (blue), 330 K (olive), and 300 K (magenta), and the position along the track (to the right and upwards) reflects the relative normalization of the BB and the galaxy template, which we parameterize using  $f_{\text{BB},10\mu\text{m}}$ , the fraction of the total flux emitted from the blackbody at  $10\mu\text{m}$ . In the right panels we show example SEDs for both the 300 K (top) and 400 K (bottom) examples, with the galaxy template in blue, the BB in red, and the total flux in green. We overplot the W1, W2, and W3 fluxes, and provide the W1 – W2 and W2 – W3 colors in each panel.

From the tracks and SEDs in Figure 7, we can see how the sequence of dwarf galaxies arises in *WISE* color space. At a fixed BB normalization, as the temperature of the hottest dust in a given galaxy increases, galaxies move upward and to the left, satisfying the Stern et al. (2012), and potentially the Jarrett et al. (2011) AGN selection criteria. Alternately, at a fixed BB temperature, as the normalization of the BB template increases, objects move upward and to the right. While a BB is a simplistic approximation of the dust emission observed in

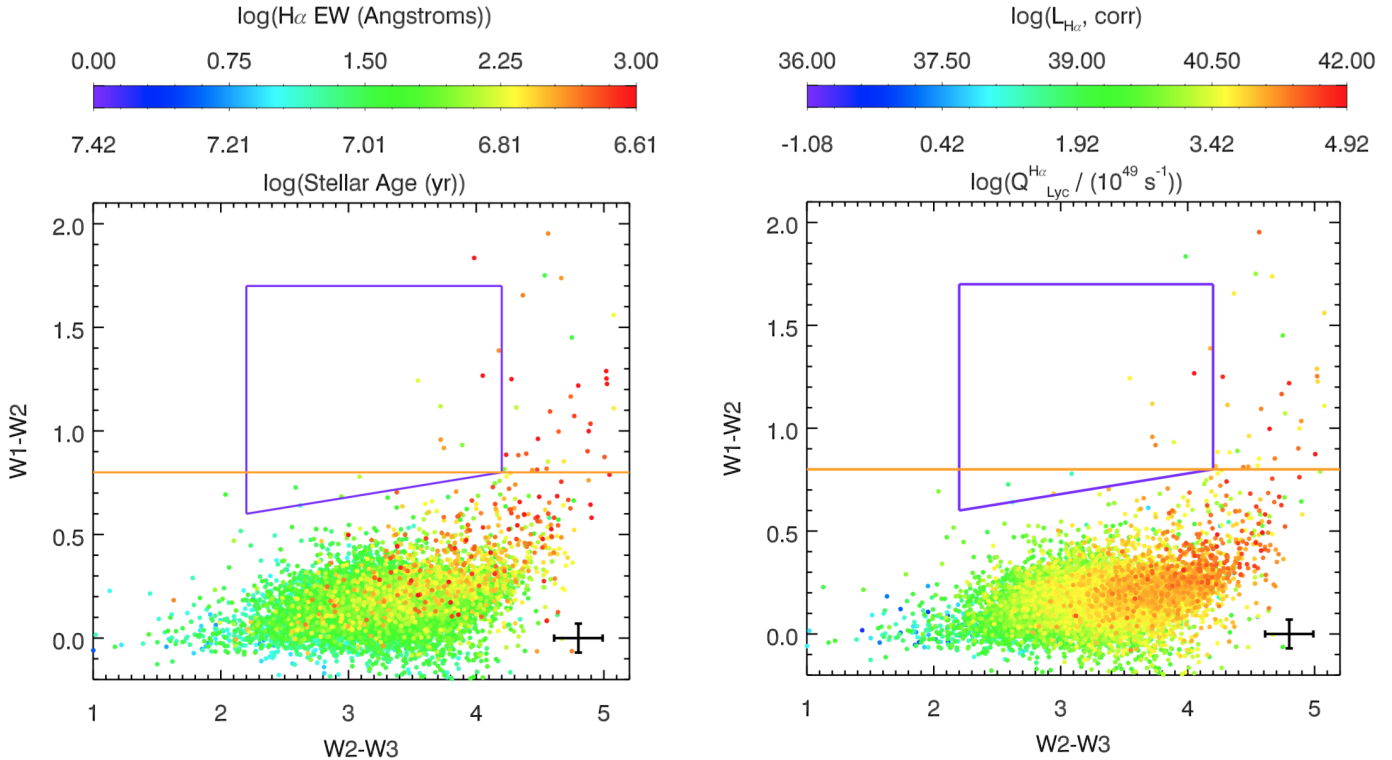


FIG. 6.— (Left) *WISE* color-color diagram for the star-forming dwarf galaxies in our sample, colored by the EW of the H $\alpha$  emission line. The color bar indicates the derived ages of the stellar populations estimated from the H $\alpha$  EW and Starburst99 models. (Right) *WISE* color-color diagram for the star-forming objects in our sample, colored by the extinction-corrected luminosity of the H $\alpha$  emission line. The color bar also provides an estimate for the rate of ionizing photons ( $Q_{Lyc}$ ) for these objects, as described in Equation 2. We also plot the median W1 – W2 and W2 – W3 uncertainties with the error bars in the bottom-right corner of each panel.

the infrared, our model does replicate the observed range in W1 – W2 and W2 – W3 colors for the dwarf galaxies. We emphasize that our model lacks PAH emission, which may significantly change the observed colors, although lower PAH abundance has been found in low-metallicity, high-sSFR dwarf galaxies (Wu et al. 2005; Madden et al. 2006; Engelbracht et al. 2008; Galliano et al. 2008; Rémy-Ruyer et al. 2015). The BB temperatures from our models are consistent with those estimated for dust heated from star-formation in dwarf galaxies in the literature (Johnson et al. 2004; Engelbracht et al. 2005; Jackson et al. 2006; Reines et al. 2008). In addition, as the *WISE* wavelength coverage does not extend to the far-infrared, and we cannot quantify cooler dust in these galaxies. We further discuss the implications of these results in Section 4.

### 3.2.3. Mid-IR selected AGN Candidates

While our results indicate that the majority of star-forming dwarf galaxies lie outside of the commonly-used *WISE* AGN selection boxes, there are potential IR-selected AGN candidates that we want to highlight. We find only 10 dwarf star-forming galaxies with *WISE* colors that put them in the Jarrett et al. (2011) AGN selection box. We present SDSS thumbnails for these objects in Figure 8. These objects span a range in optical color, but are on average bluer than the full sample of dwarf galaxies (e.g., see Figure 4). Three out of the ten objects do not have significant ( $SNR > 3$ ) W4 photometry (NSAID 93798, 109919, and 117162), as would be expected for an AGN. Two of these objects, NSAID 109919

and 93798, have low surface brightness, and do not show strong photometric evidence for a central nuclear source. NSA 93978 was presented by Secret et al. (2015) who demonstrated that this galaxy was detected by *XMM-Newton* with a luminosity of  $L_{2-10keV} = 2.4 \times 10^{40}$  erg s $^{-1}$ . We further discuss this object in Section 3.4. For the remainder of the objects, their morphologies are either compact blue nuggets (i.e. 98135), objects with blue cores and extended features (4610, and 118025), or objects with evidence for disks and nuclear cores (6205, 57649, and 151888).

### 3.3. Galaxies Without Optical Emission Line Flux Measurements

There are a number of dwarf galaxies in our sample (4,469 objects) with low S/N detections of the emission lines in existing SDSS spectra or no spectroscopic information in the NSA. From this subsample, we initially found 68 objects that fall into the Jarrett et al. (2011) selection box. We examined these objects to explore whether they had any alternate spectroscopic information: many have SDSS DR12 spectra which allowed us to determine that the NSA redshifts (and therefore masses) were incorrect for these objects, and they are likely unobscured quasars at  $z \sim 1 - 2$ . There are two objects, NSA IDs 110100 and 172349, which appear to be a chance alignment of a dwarf galaxy and a background quasar. After removing any quasar contaminants, we are left with only 25 potential IR-selected AGN dwarf galaxy candidates, and we show their SDSS and *WISE* thumbnails in Figures 10, 11, and 12 in the Appendix. We note

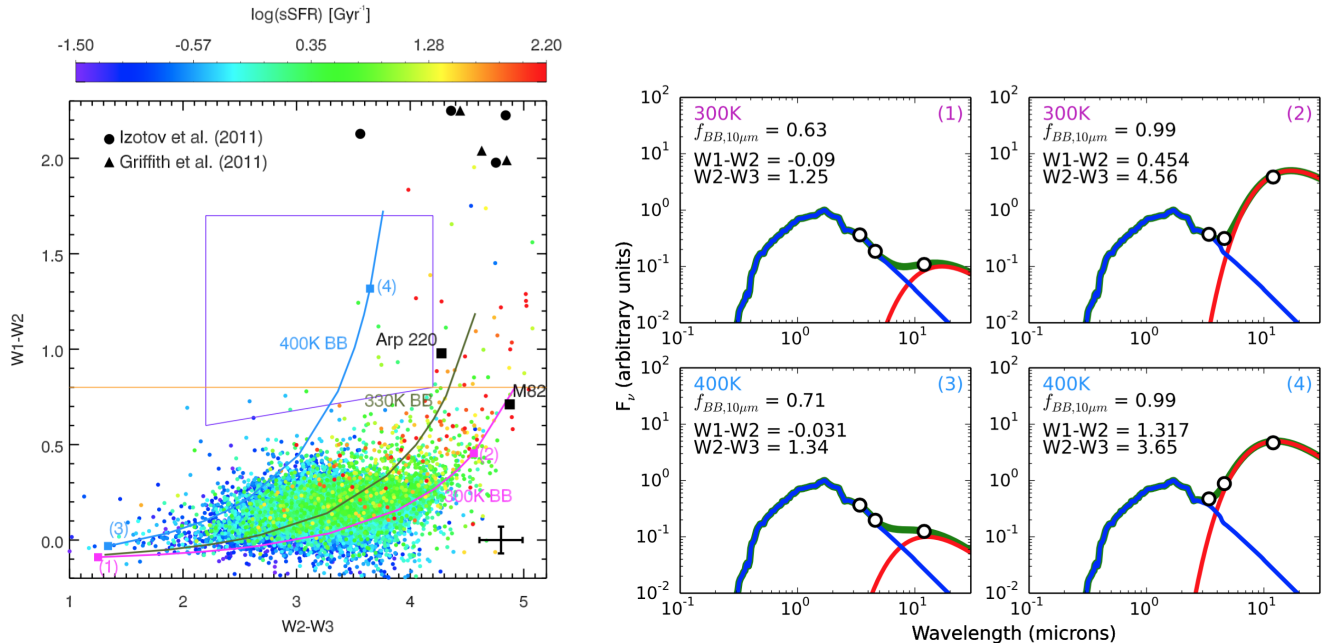


FIG. 7.— *WISE* color-color diagram for the BPT-selected star-forming dwarf galaxies. The objects are colored by sSFR as shown in the colorbar above the figure. Those objects with the highest sSFR values are found to the right and upwards on the diagram. We also plot two samples of objects with extreme *WISE*  $W1 - W2$  colors from Izotov et al. (2011) and Griffith et al. (2011), which appear to be a natural extension of the sequence of dwarf galaxies that extends from the bottom left corner to the top right corner. On top of the sequence, we plot color tracks generated by adding a blackbody to an Assef et al. (2010) elliptical galaxy template (an elliptical galaxy template was chosen as the IR emission in this template is lacking in dust emission which we model with the blackbody) at  $z = 0$ . The different colors (magenta is 300 K, olive is 330 K, and blue is 400 K) represent different blackbody temperatures, and the sequence is generated by varying the ratio of the total IR luminosity of the black body with respect to the elliptical template, as shown in the sample SEDs plotted on the right panels. The colored numbers in the top right of each panel correspond to the positions on the left color-color diagram. In each panel on the right we also provide  $f_{BB,10\mu m}$ , the fraction of the total flux that is emitted by the BB at  $10\mu m$ . The dwarf galaxies seem to trace a sequence in color space represented by more luminous dust emission, with a scatter in the sequence that arises due to different maximum dust temperature. We also plot the median  $W1 - W2$  and  $W2 - W3$  uncertainties with the error bars in the bottom-right corner of the left panel.

that two of these objects, NSA IDs 135305 and 150927, have poor  $W3$  photometric fits (for these objects, the *WISE*  $w3rchi2$  value, the  $\chi^2$  of the  $W3$  profile fitting, is  $W3rchi2 \geq 2$ ), and their  $W3$  flux might be underpredicted, leading to these objects being bluer in  $W2 - W3$  color. Many of the dwarf galaxies do not have significant  $W4$  detections. We would expect  $W4$  detections from the power-law emission typically associated with an AGN, as seen for the BPT-AGNs in Figure 2. While the sizes and  $g-r$  colors for these objects span a similar range as what was measured for the full sample of BPT star-forming objects in Figures 4 and 5, many are either optically redder or physically larger than the star-forming dwarf galaxies with red  $W1 - W2$  colors. Optical spectroscopy is necessary to better understand these systems.

We list the NSAID, SDSS ID, redshift, optical color, and *WISE* colors for all of the AGN candidates (using the Jarrett et al. (2011) selection box) in Table 1. Furthermore, we plot all the NSA dwarf galaxies that have *WISE* colors placing them inside the Jarrett et al. (2011) selection box in Figure 9, with the points colored by their optical properties. We note that these objects do not span the entire Jarrett et al. (2011) selection space, but cluster near the right and bottom of the box.

### 3.4. Comparison to Recent Searches for AGNs in Dwarf Galaxies using Mid-IR Colors

Recently, Satyapal et al. (2014) and Sartori et al. (2015) used *WISE* data to search for the presence of

AGNs in dwarf and bulgeless galaxies. These objects were used to draw conclusions about the AGN population that would be missed in optical and X-ray surveys. Of the 30 AGN candidates using the Jarrett et al. (2011) selection box and presented in Satyapal et al. (2014), only one object is in the mass and redshift range probed by our analysis here (the others are either at higher masses or higher redshifts), and it is found in our sample of star-forming dwarfs in the Jarrett et al. (2011) box (NSA ID 93798). Secret et al. (2015) measured an X-ray luminosity from *XMM-Newton* observations (extracted with a  $\sim 15''$  aperture) of  $L_{2-10keV} = 2.4 \times 10^{40}$  erg  $s^{-1}$  for this object, and claim that the  $W1 - W2$  color is strongly indicative of AGN activity. While this object is indeed in the Jarrett et al. (2011) selection box, given the median uncertainties on the *WISE* photometry, its infrared colors are consistent with this object potentially being scattered from the primary locus of star-forming galaxies and it does not have strong power law to longer infrared wavelengths as expected for an AGN.

Sartori et al. (2015) presented a sample of 83 objects with photometry placing them in the Jarrett et al. (2011) selection box, using data from the older *WISE* All-Sky data release. These authors only required  $SNR > 2$  for detections in the  $W1$ ,  $W2$ , and  $W3$  photometric bands. We cross-matched against the more up-to-date AllWISE selection, and using a  $SNR$  cut of 3.0, we find that only 34 objects ( $\sim 41\%$ ) continue to fall inside the Jarrett et al.

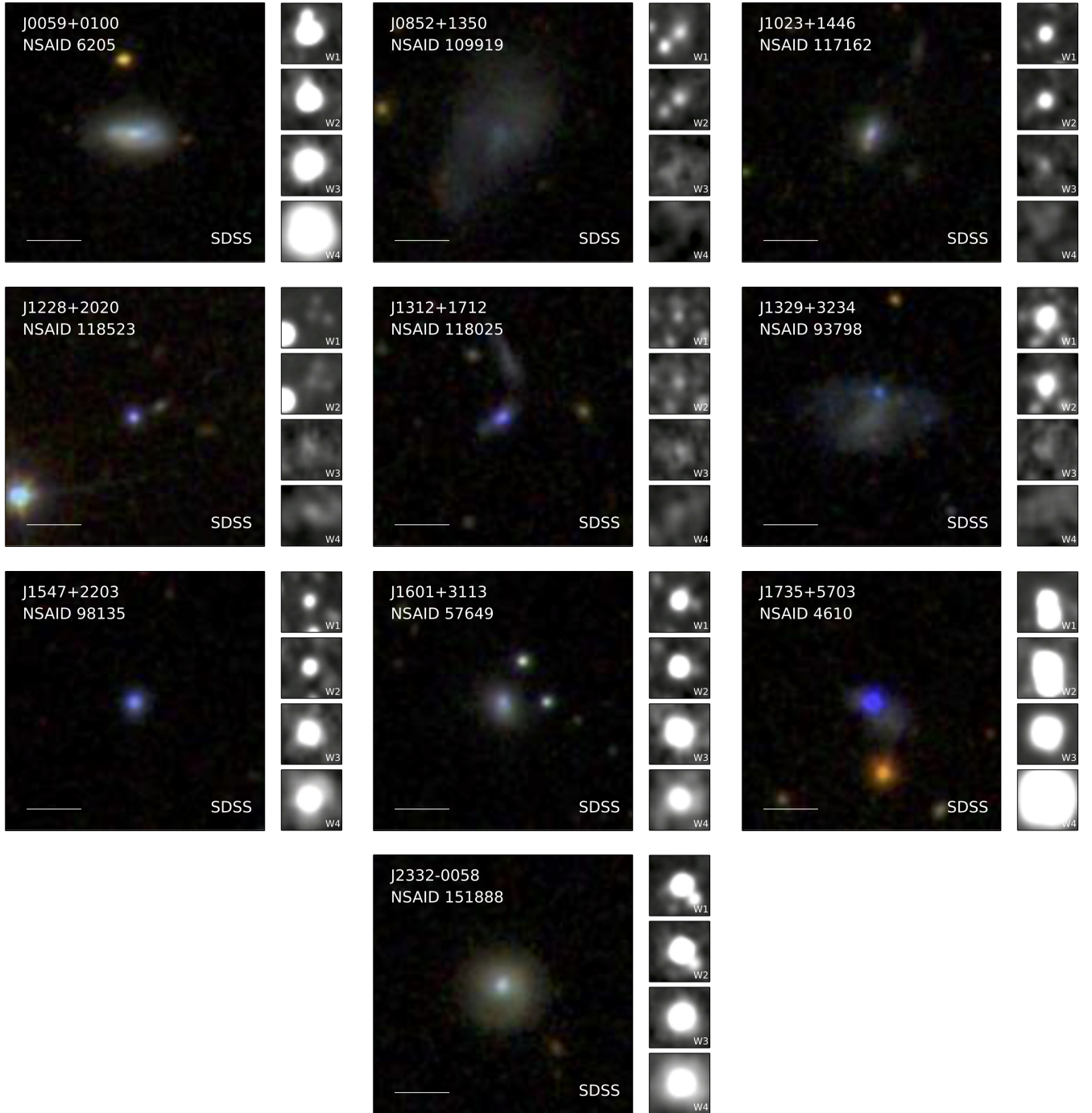


FIG. 8.— SDSS and *WISE* thumbnails for the *WISE*-selected (Jarrett et al. 2011) AGN candidates in the star-forming region of the BPT diagram. In each panel, north is up, and east is to the left, and the bar in the bottom left of each SDSS panel is  $10''$  in length. Both the SDSS and *WISE* thumbnails are  $48''$  on a side. At the median redshift of our sample,  $z = 0.03$ ,  $1'' = 0.6$  kpc.

selection box<sup>5</sup>. Of these 34 objects, only 15 are in our parent sample of dwarf galaxies. The remaining 19 objects are either not in the NSA because their redshifts are greater than 0.055, or are in the NSA but not classified as dwarf galaxies by our mass criterion. Looking closer at these 15 dwarf galaxies, 10 are found in Table 1 (NSA IDs

4610, 6205, 10311, 53934, 57649, 93798, 109919, 117162, 118025, and 118523), four of the 15 are BPT-selected AGNs or composite galaxies (NSA IDs 10779, 79874, 124050, and 125318), and one is the previously discussed quasar contaminant (NSA ID 110100). One object that was listed as a Stern et al. (2012) candidate but not a Jarrett et al. (2011) candidate in Sartori et al. (2015) moved into the Jarrett et al. (2011) selection box with the updated AllWISE photometry (NSA ID 98135), and one object we have listed in Table 1 does not appear in

<sup>5</sup> All 83 of the objects in the Sartori et al. (2015) sample have updated AllWISE W1 and W2 photometry with  $\text{SNR} > 3.0$ , but 26 of the objects have W3 photometry with  $\text{SNR} < 3$ , only 10 of which have  $2 < \text{SNR} < 3$ .

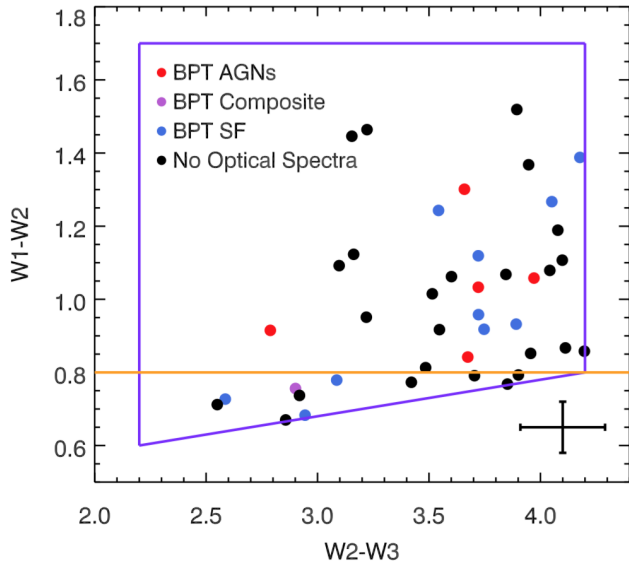


FIG. 9.— *WISE* color-color diagram focusing on those objects that fall in the Jarrett et al. (2011) selection box. We plot the positions of the Reines et al. (2013) dwarf AGNs in red, dwarf composite objects in purple, the BPT SF objects in blue, and the galaxies without SDSS spectroscopic information in black. We also plot the median  $W1 - W2$  and  $W2 - W3$  uncertainties with the error bars in the bottom-right corner.

Sartori et al. (2015) (NSA ID 151888).

### 3.5. The Feasibility of Detecting Supermassive Black Holes in Dwarf Galaxies with *WISE*

Finding evidence for AGNs in dwarf galaxies is challenging as AGNs at a given accretion rate have lower bolometric luminosities due to the smaller masses of the central black holes, making them harder to observe above the emission due to star formation in their host galaxies. It has been shown using common emission line AGN selection techniques that there is a strong bias against finding AGNs in low mass galaxies for this reason (Aird et al. 2012; Bongiorno et al. 2012; Hainline et al. 2012; Trump et al. 2015). To that end, we sought to explore the range of black hole masses in potential AGNs in dwarf galaxies that are detectable using *WISE* colors, following a similar discussion in Reines et al. (2013).

We calculate the minimum black hole detectable in the scenario where the AGN flux must be above some median flux from star formation at 3–4  $\mu\text{m}$ . Assuming that the bulk of the objects with  $W1 - W2 < 0.5$  have *WISE* fluxes that are dominated by dust heated from star formation, we calculate the median  $W1$  and  $W2$  fluxes for all of these objects after shifting them to the median redshift of our sample. We do not perform this calculation using the  $W3$  fluxes, as the differences in cold dust temperatures across the sample is more obvious at 12  $\mu\text{m}$  than at the shorter wavelengths. We calculate median  $W1$  and  $W2$  fluxes of 382 and 243  $\mu\text{Jy}$  respectively. From here, we use the low resolution AGN spectral template from Assef et al. (2010) to estimate the AGN bolometric luminosity for an object at the median redshift of  $z \sim 0.03$  given these flux limits. We note that this template was derived using more luminous AGNs, and the actual relationship between the IR and bolometric luminosities may vary for lower-mass black holes. We derive

minimum black hole masses of  $1 - 3 \times 10^3 M_{\odot}$ , if we assume that the black hole is accreting at the Eddington limit, where  $L_{\text{Edd}} = 1.3 \times 10^{38} (M_{\text{BH}}/M_{\odot}) \text{ erg s}^{-1}$ . However, black hole accretion at such high levels is quite rare (Schulze & Wisotzki 2010), and we also calculate that a black hole with mass  $10^5 M_{\odot}$  (similar to the masses of the BHs measured in dwarf galaxies in Reines et al. 2013; Baldassare et al. 2015) would only need to radiate at 1–6% of its Eddington luminosity to be observed given the median flux from star formation in our sample.

## 4. DISCUSSION AND CONCLUSIONS

To better understand the birth and growth of supermassive black holes, it is fundamentally important to find evidence for AGN activity in low mass dwarf galaxies. Here, we looked at the mid-IR properties of a sample of dwarf galaxies at  $z < 0.055$  to explore the use of *WISE* colors to select for AGN activity. We used the most up-to-date AllWISE photometry and individually inspected each candidate AGN to select a sample that is significantly smaller than previous samples of IR-selected AGNs in dwarf galaxies.

Our main conclusions are:

- The majority of optically-selected AGNs in dwarf galaxies have IR colors that are dominated by their host galaxies.
- Dwarf galaxies with the reddest *WISE* colors are compact, blue galaxies with young stellar ages and high sSFRs. Dwarf galaxies with extreme star-formation are capable of heating dust to temperatures producing  $W1 - W2 > 0.8$ , (e.g. Stern et al. 2012), and this single color cut alone should not be used to select AGNs in dwarf galaxies.
- We provide a sample of 41 dwarf galaxies in the NSA which have *WISE* colors in the Jarrett et al. (2011) AGN selection box, 6 of which have optical spectroscopic evidence for an AGN (Reines et al. 2013). While the majority of the objects in our sample have been included in previous samples of *WISE*-selected dwarf galaxy AGN candidates, our sample is much smaller due to the updated *WISE* photometry, more conservative selection criteria and SNR thresholds, and the removal of spurious candidates. We caution that follow-up observations are necessary to confirm the presence of active massive black holes in the other 35 objects.

From our analysis, optically blue, high sSFR dwarfs with young starbursts and associated high ionizing fluxes can have red mid-IR colors that could be mistaken for AGN activity, particularly if using a simple  $W1 - W2$  color cut. While these objects have a population of young stars that can heat dust to temperatures which result in red  $W1 - W2$  colors ( $W1 - W2 > 0.5 - 0.6$ ), they primarily have *very* red  $W2 - W3$  colors ( $W2 - W3 > 4.2$ ), which is less extreme, but similar to the  $W2 - W3$  colors seen for the dwarf star-forming galaxies from Izotov et al. (2011).

AGNs, which can heat dust to even higher temperatures, are predominantly found in a different region of *WISE* color-color space, and we only find 10 optically-selected star-forming dwarf galaxies that would be classified as an AGN by the Jarrett et al. (2011) selection

criteria. Of those objects, only 5 have strong W3 and W4 fluxes as would be expected for an AGN. In addition, these objects are consistent with the overall trend of star-forming galaxies in *WISE* color space, and these objects could represent an extreme star-forming population that has scattered into the Jarrett et al. (2011) selection box. We also found 25 additional dwarf galaxies that fell into the Jarrett et al. (2011) box that do not have optical spectroscopy, or their SDSS emission lines were not strong enough to classify them on the BPT diagram. We include them as candidates, but we caution against using the mid-IR colors of these objects alone to classify them as AGNs; follow-up observations at optical or X-ray wavelengths would be helpful to understand the nature of their IR emission.

Overall, it is important to use both W1 – W2 and W2 – W3 colors when selecting candidate AGNs in dwarf galaxies, as any selection of AGNs in dwarf galaxies that only uses W1 – W2 color (for instance, the selection method of Stern et al. 2012, which has been demonstrated to be reliable at higher masses) will include a large amount of contamination from dwarf star-forming galaxies. Starting with the BPT star-forming galaxies discussed in Section 3.2, we find that 42 dwarf galaxies have  $W1 - W2 > 0.8$  (compared to only 10 in the Jarrett et al. (2011) selection box), while 183 objects have  $W1 - W2 > 0.5$ . This contamination from star-forming dwarf galaxies is likely the cause of the observed rise in the fraction of AGN candidates at lower galaxy masses in Satyapal et al. (2014) and Sartori et al. (2015). While we certainly cannot rule out the presence of AGNs in the optically-selected star-forming dwarf galaxies with red *WISE* colors, the systematic correlations between star formation properties and infrared colors leads us to conclude that the infrared emission is unlikely to be powered by AGNs. Furthermore, the majority of known optically-selected AGNs in dwarf galaxies do not dominate the *WISE* colors.

Our results are consistent with evidence in the literature that the ionizing UV radiation from young stars is one of the primary sources of dust heating in low-metallicity dwarf galaxies (Izotov et al. 2014). Both *IRAS* and *Spitzer* observations demonstrated that dwarf galaxies have evidence for large quantities of hot dust (Helou 1986; Hunter et al. 1989; Melisse & Israel 1994; Rosenberg et al. 2006; Cannon et al. 2006). In addition, it has been shown that the IR SED peak of dwarf galaxies is broader, which is often explained as resulting from dust at higher temperatures than what is ob-

served in more massive galaxies (Boselli et al. 2012; Smith et al. 2012; Rémy-Ruyer et al. 2013, 2015; Ciesla et al. 2014). The temperatures from the tracks in Figure 7 for the hot dust that would be necessary to produce the observed *WISE* colors has been observed in local low-metallicity galaxies from *Spitzer*  $8\mu\text{m}$  observations (Engelbracht et al. 2005; Jackson et al. 2006), and even hotter dust has been invoked to explain the near-IR excesses observed in the dwarf galaxies SBS 0335-052 (Reines et al. 2008) and Haro 3 (Johnson et al. 2004). Recently, in an analysis of the infrared properties of a large sample of low-metallicity dwarf galaxies, Rémy-Ruyer et al. (2015) demonstrated that the dust SED for these galaxies peaks at shorter wavelengths as compared to higher-metallicity systems, which they attribute to a clumpy interstellar medium that allows for a wider range of dust temperatures. In addition, the lower-metallicity dust will attenuate the light from young stars less, and the dust can then be heated deeper within individual molecular clouds. Cormier et al. (2015) used *Herschel* PACS spectroscopy of low-metallicity dwarf galaxies to provide evidence that the interstellar medium in these galaxies is more porous than in metal-rich galaxies, leading to a larger fraction of the stellar UV radiation heating dust. These results are supported by modeling by Hirashita & Hunt (2004), which found that dust temperature and dust luminosity is higher in dense, compact, low-metallicity star-forming regions.

Support for AER was provided by NASA through Hubble Fellowship grant HST-HF2-51347.001-A awarded by the Space Telescope Science Institute, which is operated by the Association of Universities for Research in Astronomy, Inc., for NASA, under contract NAS 5-26555. The work of DS was carried out at the Jet Propulsion Laboratory, California Institute of Technology, under a contract with NASA. We are grateful to the entire SDSS collaboration for providing the data that made this work possible, and to Michael Blanton and all those involved in creating the NASA-Sloan Atlas. This publication makes use of data products from the Wide-field Infrared Survey Explorer, which is a joint project of the University of California, Los Angeles, and the Jet Propulsion Laboratory/California Institute of Technology, and NEOWISE, which is a project of the Jet Propulsion Laboratory/California Institute of Technology. *WISE* and NEOWISE are funded by the National Aeronautics and Space Administration.

## REFERENCES

- Aihara, H., Allende Prieto, C., An, D., Anderson, S. F., Aubourg, É., Balbinot, E., Beers, T. C., Berlind, A. A., Bickerton, S. J., Bizyaev, D., Blanton, M. R., Bochanski, J. J., Bolton, A. S., Bovy, J., Brandt, W. N., Brinkmann, J., Brown, P. J., & et al. 2011, *ApJS*, 193, 29
- Aird, J., Coil, A. L., Moustakas, J., Blanton, M. R., Burles, S. M., Cool, R. J., Eisenstein, D. J., Smith, M. S. M., Wong, K. C., & Zhu, G. 2012, *ApJ*, 746, 90
- Ashby, M. L. N., et al. 2009, *ApJ*, 701, 428
- Assef, R. J., Kochanek, C. S., Brodwin, M., Cool, R., Forman, W., Gonzalez, A. H., Hickox, R. C., Jones, C., Le Floch, E., Moustakas, J., Murray, S. S., & Stern, D. 2010, *ApJ*, 713, 970
- Baldassare, V. F., Reines, A. E., Gallo, E., & Greene, J. E. 2015, *ApJ*, 809, L14
- Baldassare, V. F., Reines, A. E., Gallo, E., Greene, J. E., Graur, O., Geha, M., Hainline, K., Carroll, C. M., & Hickox, R. C. 2016, *ArXiv e-prints*
- Baldwin, J. A., Phillips, M. M., & Terlevich, R. 1981, *PASP*, 93, 5
- Barth, A. J., Ho, L. C., Rutledge, R. E., & Sargent, W. L. W. 2004, *ApJ*, 607, 90
- Begelman, M. C., Volonteri, M., & Rees, M. J. 2006, *MNRAS*, 370, 289
- Bell, E. F., McIntosh, D. H., Katz, N., & Weinberg, M. D. 2003, *ApJS*, 149, 289
- Bessiere, P. S., Tadhunter, C. N., Ramos Almeida, C., & Villar Martín, M. 2012, *MNRAS*, 426, 276
- Blanton, M. R., Kazin, E., Muna, D., Weaver, B. A., & Price-Whelan, A. 2011, *AJ*, 142, 31
- Blanton, M. R. & Roweis, S. 2007, *AJ*, 133, 734

- Bongiorno, A., Merloni, A., Brusa, M., Magnelli, B., Salvato, M., Mignoli, M., Zamorani, G., Fiore, F., Rosario, D., Mainieri, V., Hao, H., Comastri, A., Vignali, C., Balestra, I., Bardelli, S., Berta, S., Civano, F., Kampczyk, P., Le Floch, E., Lusso, E., Lutz, D., Pozzetti, L., Pozzi, F., Riguccini, L., Shankar, F., & Silverman, J. 2012, *MNRAS*, 427, 3103
- Boselli, A., Ciesla, L., Cortese, L., Buat, V., Boquien, M., Bendo, G. J., Boissier, S., Eales, S., Gavazzi, G., Hughes, T. M., Pohlen, M., Smith, M. W. L., Baes, M., Bianchi, S., Clements, D. L., Cooray, A., Davies, J., Gear, W., Madden, S., Magrini, L., Panuzzo, P., Remy, A., Spinoglio, L., & Zibetti, S. 2012, *A&A*, 540, A54
- Bromm, V. & Yoshida, N. 2011, *ARA&A*, 49, 373
- Bruzual, G. & Charlot, S. 2003, *MNRAS*, 344, 1000
- Cannon, J. M., Walter, F., Armus, L., Bendo, G. J., Calzetti, D., Draine, B. T., Engelbracht, C. W., Helou, G., Kennicutt, Jr., R. C., Leitherer, C., Roussel, H., Bot, C., Buckalew, B. A., Dale, D. A., de Blok, W. J. G., Gordon, K. D., Hollenbach, D. J., Jarrett, T. H., Meyer, M. J., Murphy, E. J., Sheth, K., & Thornley, M. D. 2006, *ApJ*, 652, 1170
- Ciesla, L., Boquien, M., Boselli, A., Buat, V., Cortese, L., Bendo, G. J., Heinis, S., Galametz, M., Eales, S., Smith, M. W. L., Baes, M., Bianchi, S., De Looze, I., di Serego Alighieri, S., Galliano, F., Hughes, T. M., Madden, S. C., Pierini, D., Rémy-Ruyer, A., Spinoglio, L., Vaccari, M., Viaene, S., & Vlahakis, C. 2014, *A&A*, 565, A128
- Cluver, M. E., Jarrett, T. H., Hopkins, A. M., Driver, S. P., Liske, J., Gunawardhana, M. L. P., Taylor, E. N., Robotham, A. S. G., Alpaslan, M., Baldry, I., Brown, M. J. I., Peacock, J. A., Popescu, C. C., Tuffs, R. J., Bauer, A. E., Bland-Hawthorn, J., Colless, M., Holwerda, B. W., Lara-López, M. A., Leschinski, K., López-Sánchez, A. R., Norberg, P., Owers, M. S., Wang, L., & Wilkins, S. M. 2014, *ApJ*, 782, 90
- Condon, J. J. 1992, *ARA&A*, 30, 575
- Cormier, D., Madden, S. C., Lebouteiller, V., Abel, N., Hony, S., Galliano, F., Rémy-Ruyer, A., Bigiel, F., Baes, M., Boselli, A., Chevance, M., Cooray, A., De Looze, I., Doublier, V., Galametz, M., Hughes, T., Karczewski, O. L., Lee, M.-Y., Lu, N., & Spinoglio, L. 2015, *A&A*, 578, A53
- Cutri, R. M. & et al. 2013, *VizieR Online Data Catalog*, 2328
- Dong, X.-B., Ho, L. C., Yuan, W., Wang, T.-G., Fan, X., Zhou, H., & Jiang, N. 2012, *ApJ*, 755, 167
- Donley, J. L., Rieke, G. H., Pérez-González, P. G., & Barro, G. 2008, *ApJ*, 687, 111
- Ellison, S. L., Patton, D. R., Mendel, J. T., & Scudder, J. M. 2011, *MNRAS*, 418, 2043
- Engelbracht, C. W., Gordon, K. D., Rieke, G. H., Werner, M. W., Dale, D. A., & Latter, W. B. 2005, *ApJ*, 628, L29
- Engelbracht, C. W., Rieke, G. H., Gordon, K. D., Smith, J.-D. T., Werner, M. W., Moustakas, J., Willmer, C. N. A., & Vanzi, L. 2008, *ApJ*, 678, 804
- Ferrarese, L. & Merritt, D. 2000, *ApJ*, 539, L9
- Filippenko, A. V. & Ho, L. C. 2003, *ApJ*, 588, L13
- Filippenko, A. V. & Sargent, W. L. W. 1989, *ApJ*, 342, L11
- Freitag, M., Gürkan, M. A., & Rasio, F. A. 2006, *MNRAS*, 368, 141
- Galliano, F., Dwek, E., & Chantal, P. 2008, *ApJ*, 672, 214
- Gebhardt, K., Bender, R., Bower, G., Dressler, A., Faber, S. M., Filippenko, A. V., Green, R., Grillmair, C., Ho, L. C., Kormendy, J., Lauer, T. R., Magorrian, J., Pinkney, J., Richstone, D., & Tremaine, S. 2000, *ApJ*, 539, L13
- Giersz, M., Leigh, N., Hupki, A., Lützgendorf, N., & Askar, A. 2015, *MNRAS*, 454, 3150
- Goswami, S., Umbreit, S., Bierbaum, M., & Rasio, F. A. 2012, *ApJ*, 752, 43
- Greene, J. E. & Ho, L. C. 2004, *ApJ*, 610, 722
- . 2007, *ApJ*, 670, 92
- Griffith, R. L., Tsai, C.-W., Stern, D., Blain, A., Eisenhardt, P. R. M., Harrison, F., Jarrett, T. H., Madsen, K., Stanford, S. A., Wright, E. L., Wu, J., Wu, Y., & Yan, L. 2011, *ApJ*, 736, L22
- Gürkan, M. A., Freitag, M., & Rasio, F. A. 2004, *ApJ*, 604, 632
- Haehnelt, M. G. & Rees, M. J. 1993, *MNRAS*, 263, 168
- Hainline, K. N., Hickox, R. C., Carroll, C. M., Myers, A. D., DiPompeo, M. A., & Trouille, L. 2014, *ApJ*, 795, 124
- Hainline, K. N., Shapley, A. E., Greene, J. E., Steidel, C. C., Reddy, N. A., & Erb, D. K. 2012, *ApJ*, 760, 74
- Helou, G. 1986, *ApJ*, 311, L33
- Hickox, R. C., Jones, C., Forman, W. R., Murray, S. S., Brodwin, M., Brown, M. J. I., Eisenhardt, P. R., Stern, D., Kochanek, C. S., Eisenstein, D., Cool, R. J., Jannuzi, B. T., Dey, A., Brand, K., Gorjian, V., & Caldwell, N. 2007, *ApJ*, 671, 1365
- Hirashita, H. & Hunt, L. K. 2004, *A&A*, 421, 555
- Hopkins, P. F., Hernquist, L., Cox, T. J., & Kereš, D. 2008, *ApJS*, 175, 356
- Hunter, D. A., Gallagher, III, J. S., Rice, W. L., & Gillett, F. C. 1989, *ApJ*, 336, 152
- Izotov, Y. I., Guseva, N. G., Fricke, K. J., & Henkel, C. 2011, *A&A*, 536, L7
- Izotov, Y. I., Guseva, N. G., Fricke, K. J., Krügel, E., & Henkel, C. 2014, *A&A*, 570, A97
- Izotov, Y. I., Lipovetsky, V. A., Chaffee, F. H., Foltz, C. B., Guseva, N. G., & Kniazev, A. Y. 1997, *ApJ*, 476, 698
- Jackson, D. C., Cannon, J. M., Skillman, E. D., Lee, H., Gehrz, R. D., Woodward, C. E., & Polomski, E. 2006, *ApJ*, 646, 192
- Jarrett, T. H., Cohen, M., Masci, F., Wright, E., Stern, D., Benford, D., Blain, A., Carey, S., Cutri, R. M., Eisenhardt, P., Lonsdale, C., Mainzer, A., Marsh, K., Padgett, D., Petty, S., Ressler, M., Skrutskie, M., Stanford, S., Surace, J., Tsai, C. W., Wheelock, S., & Yan, D. L. 2011, *ApJ*, 735, 112
- Johnson, K. E., Indebetouw, R., Watson, C., & Kobulnicky, H. A. 2004, *AJ*, 128, 610
- Kauffmann, G., Heckman, T. M., Tremonti, C., Brinchmann, J., Charlot, S., White, S. D. M., Ridgway, S. E., Brinkmann, J., Fukugita, M., Hall, P. B., Ivezić, Z., Richards, G. T., & Schneider, D. P. 2003, *MNRAS*, 346, 1055
- Kennicutt, R. C. & Evans, N. J. 2012, *ARA&A*, 50, 531
- Kewley, L. J., Dopita, M. A., Leitherer, C., Davé, R., Yuan, T., Allen, M., Groves, B., & Sutherland, R. 2013, *ApJ*, 774, 100
- Kewley, L. J., Dopita, M. A., Sutherland, R. S., Heisler, C. A., & Trevena, J. 2001, *ApJ*, 556, 121
- Kormendy, J. & Ho, L. C. 2013, *ARA&A*, 51, 511
- Kormendy, J. & Richstone, D. 1995, *ARA&A*, 33, 581
- Koss, M., Mushotzky, R., Veilleux, S., & Winter, L. 2010, *ApJ*, 716, L125
- Lacy, M., Ridgway, S. E., Gates, E. L., Nielsen, D. M., Petric, A. O., Sajina, A., Urrutia, T., Cox Drews, S., Harrison, C., Seymour, N., & Storrie-Lombardi, L. J. 2013, *ApJS*, 208, 24
- Lacy, M., Storrie-Lombardi, L. J., Sajina, A., Appleton, P. N., Armus, L., Chapman, S. C., Choi, P. I., Fadda, D., Fang, F., Frayer, D. T., Heinrichsen, I., Helou, G., Im, M., Marleau, F. R., Masci, F., Shupe, D. L., Soifer, B. T., Surace, J., Teplitz, H. I., Wilson, G., & Yan, L. 2004, *ApJS*, 154, 166
- Leitherer, C., Schaerer, D., Goldader, J. D., Delgado, R. M. G., Robert, C., Kune, D. F., de Mello, D. F., Devost, D., & Heckman, T. M. 1999, *ApJS*, 123, 3
- Lemons, S. M., Reines, A. E., Plotkin, R. M., Gallo, E., & Greene, J. E. 2015, *ApJ*, 805, 12
- Lodato, G. & Natarajan, P. 2006, *MNRAS*, 371, 1813
- Lützgendorf, N., Kissler-Patig, M., Gebhardt, K., Baumgardt, H., Kruijssen, D., Noyola, E., Neumayer, N., de Zeeuw, T., Feldmeier, A., van der Helm, E., Pelupessy, I., & Zwart, S. P. 2016, in *IAU Symposium*, Vol. 312, IAU Symposium, ed. Y. Meiron, S. Li, F.-K. Liu, & R. Spurzem, 181–188
- Madden, S. C., Galliano, F., Jones, A. P., & Sauvage, M. 2006, *A&A*, 446, 877
- Mateos, S., Alonso-Herrero, A., Carrera, F. J., Blain, A., Watson, M. G., Barcons, X., Baito, V., Severgnini, P., Donley, J. L., & Stern, D. 2012, *MNRAS*, 426, 3271
- Melisse, J. P. M. & Israel, F. P. 1994, *A&A*, 285
- Mendez, A. J., Coil, A. L., Aird, J., Diamond-Stanic, A. M., Moustakas, J., Blanton, M. R., Cool, R. J., Eisenstein, D. J., Wong, K. C., & Zhu, G. 2013, *ApJ*, 770, 40
- Mezcua, M., Roberts, T. P., Lobanov, A. P., & Sutton, A. D. 2015, *MNRAS*, 448, 1893
- Moran, E. C., Shahinyan, K., Sugarman, H. R., Vélez, D. O., & Eracleous, M. 2014, *AJ*, 148, 136
- O'Connor, J. A., Rosenberg, J. L., Satyapal, S., & Secrest, N. J. 2016, *MNRAS*
- O'Donnell, J. E. 1994, *ApJ*, 422, 158
- Pardo, K., Goulding, A. D., Greene, J. E., Somerville, R. S., Gallo, E., Hickox, R. C., Miller, B. P., Reines, A. E., & Silverman, J. D. 2016, *ArXiv e-prints*

- Polletta, M., Tajer, M., Maraschi, L., Trinchieri, G., Lonsdale, C. J., Chiappetti, L., Andreon, S., Pierre, M., Le Fèvre, O., Zamorani, G., Maccagni, D., Garcet, O., Surdej, J., Franceschini, A., Alloin, D., Shupe, D. L., Surace, J. A., Fang, F., Rowan-Robinson, M., Smith, H. E., & Tresse, L. 2007, *ApJ*, 663, 81
- Reines, A. E. & Deller, A. T. 2012, *ApJ*, 750, L24
- Reines, A. E., Greene, J. E., & Geha, M. 2013, *ApJ*, 775, 116
- Reines, A. E., Johnson, K. E., & Hunt, L. K. 2008, *AJ*, 136, 1415
- Reines, A. E., Plotkin, R. M., Russell, T. D., Mezcua, M., Condon, J. J., Sivakoff, G. R., & Johnson, K. E. 2014, *ApJ*, 787, L30
- Reines, A. E., Sivakoff, G. R., Johnson, K. E., & Brogan, C. L. 2011, *Nature*, 470, 66
- Reines, A. E. & Volonteri, M. 2015, *ApJ*, 813, 82
- Rémy-Ruyer, A., Madden, S. C., Galliano, F., Hony, S., Sauvage, M., Bendo, G. J., Roussel, H., Pohlen, M., Smith, M. W. L., Galametz, M., Cormier, D., Lebouteiller, V., Wu, R., Baes, M., Barlow, M. J., Boquien, M., Boselli, A., Ciesla, L., De Looze, I., Karczewski, O. L., Panuzzo, P., Spinoglio, L., Vaccari, M., & Wilson, C. D. 2013, *A&A*, 557, A95
- Rémy-Ruyer, A., Madden, S. C., Galliano, F., Lebouteiller, V., Baes, M., Bendo, G. J., Boselli, A., Ciesla, L., Cormier, D., Cooray, A., Cortese, L., De Looze, I., Doublier-Pritchard, V., Galametz, M., Jones, A. P., Karczewski, O. L., Lu, N., & Spinoglio, L. 2015, *A&A*, 582, A121
- Rosenberg, J. L., Ashby, M. L. N., Salzer, J. J., & Huang, J.-S. 2006, *ApJ*, 636, 742
- Sabater, J., Best, P. N., & Argudo-Fernández, M. 2013, *MNRAS*, 430, 638
- Salpeter, E. E. 1955, *ApJ*, 121, 161
- Sartori, L. F., Schawinski, K., Treister, E., Trakhtenbrot, B., Koss, M., Shirazi, M., & Oh, K. 2015, *MNRAS*, 454, 3722
- Satyapal, S., Secrest, N. J., McAlpine, W., Ellison, S. L., Fischer, J., & Rosenberg, J. L. 2014, *ApJ*, 784, 113
- Schulze, A. & Wisotzki, L. 2010, *A&A*, 516, A87
- Secrest, N. J., Satyapal, S., Gliozzi, M., Rothberg, B., Ellison, S. L., Mowry, W. S., Rosenberg, J. L., Fischer, J., & Schmitt, H. 2015, *ApJ*, 798, 38
- Smith, D. J. B., Dunne, L., da Cunha, E., Rowlands, K., Maddox, S. J., Gomez, H. L., Bonfield, D. G., Charlot, S., Driver, S. P., Popescu, C. C., Tuffs, R. J., Dunlop, J. S., Jarvis, M. J., Seymour, N., Symeonidis, M., Baes, M., Bourne, N., Clements, D. L., Cooray, A., De Zotti, G., Dye, S., Eales, S., Scott, D., Verma, A., van der Werf, P., Andrae, E., Auld, R., Buttiglione, S., Cava, A., Dariush, A., Fritz, J., Hopwood, R., Ibar, E., Ivison, R. J., Kelvin, L., Madore, B. F., Pohlen, M., Rigby, E. E., Robotham, A., Seibert, M., & Temi, P. 2012, *MNRAS*, 427, 703
- Stasińska, G. & Leitherer, C. 1996, *ApJS*, 107, 661
- Stern, D., Assef, R. J., Benford, D. J., Blain, A., Cutri, R., Dey, A., Eisenhardt, P., Griffith, R. L., Jarrett, T. H., Lake, S., Masci, F., Petty, S., Stanford, S. A., Tsai, C.-W., Wright, E. L., Yan, L., Harrison, F., & Madsen, K. 2012, *ApJ*, 753, 30
- Stern, D., Eisenhardt, P., Gorjian, V., Kochanek, C. S., Caldwell, N., Eisenstein, D., Brodwin, M., Brown, M. J. I., Cool, R., Dey, A., Green, P., Jannuzi, B. T., Murray, S. S., Pahre, M. A., & Willner, S. P. 2005, *ApJ*, 631, 163
- Trump, J. R., Sun, M., Zeimann, G. R., Luck, C., Bridge, J. S., Grier, C. J., Hagen, A., Juneau, S., Montero-Dorta, A., Rosario, D. J., Brandt, W. N., Ciardullo, R., & Schneider, D. P. 2015, *ApJ*, 811, 26
- van der Marel, R. P., Alves, D. R., Hardy, E., & Suntzeff, N. B. 2002, *AJ*, 124, 2639
- van Wassenhove, S., Volonteri, M., Walker, M. G., & Gair, J. R. 2010, *MNRAS*, 408, 1139
- Wright, E. L., et al. 2010, *AJ*, 140, 1868
- Wu, H., Cao, C., Hao, C.-N., Liu, F.-S., Wang, J.-L., Xia, X.-Y., Deng, Z.-G., & Young, C. K.-S. 2005, *ApJ*, 632, L79
- Yan, R. 2011, *AJ*, 142, 153
- Yan, R. & Blanton, M. R. 2012, *ApJ*, 747, 61
- York, D. G., & SDSS Collaboration. 2000, *AJ*, 120, 1579
- Zibetti, S., Charlot, S., & Rix, H.-W. 2009, *MNRAS*, 400, 1181

## APPENDIX

## THUMBNAILS OF JARRETT ET AL. IR-AGN CANDIDATES WITHOUT OPTICAL EMISSION LINE FLUX MEASUREMENTS

TABLE 1  
*WISE*-SELECTED / JARRETT ET AL. (2011) AGN CANDIDATES

NSAID	SDSS ID	$z$	$g - r$	W1	W1-W2	W2-W3
BPT-selected AGNs <sup>a</sup>						
68765	J032224.64+401119.8	0.026	0.618	14.012 ± 0.020	0.842	3.674
10779	J090613.75+561015.5	0.047	0.426	13.400 ± 0.024	1.301	3.659
125318	J095418.15+471725.1	0.033	0.448	13.859 ± 0.027	1.058	3.971
113566	J114359.58+244251.7	0.050	0.683	14.275 ± 0.028	0.915	2.788
104527	J133245.62+263449.3	0.047	0.281	13.514 ± 0.025	1.033	3.721
BPT-selected Composite Galaxies <sup>a</sup>						
79874	J152637.36+065941.6	0.0384	0.299	14.121 ± 0.026	0.756	2.901
BPT-selected Star-forming Galaxies <sup>b</sup>						
6205	J005904.10+010004.2	0.018	0.240	13.308 ± 0.024	0.932	3.891
109919	J085233.75+135028.3	0.005	0.305	15.761 ± 0.052	0.779	3.086
117162	J102345.04+144604.7	0.047	0.218	14.794 ± 0.033	0.683	2.944
118523	J122822.81+202043.6	0.049	-0.053	16.432 ± 0.074	0.918	3.747
118025	J131253.76+171231.1	0.052	-0.260	16.583 ± 0.086	0.958	3.722
93798	J132932.42+323416.9	0.016	0.252	15.297 ± 0.036	0.727	2.586
98135	J154748.99+220303.2	0.031	-0.390	15.583 ± 0.041	1.388	4.177
57649	J160135.95+311353.7	0.031	0.136	14.526 ± 0.028	1.243	3.543
4610	J173501.25+570308.8	0.047	-1.003	13.041 ± 0.029	1.267	4.051
151888	J233244.60-005847.9	0.024	0.382	13.581 ± 0.011	1.119	3.721
Galaxies Without Optical Emission Line Fluxes <sup>c</sup>						
127223	J003441.39-212928.9	0.023	0.027	15.975 ± 0.055	0.793	3.901
127548	J004206.29-093335.0	0.054	0.515	15.659 ± 0.049	1.189	4.078
128988	J011600.59+063812.9	0.008	0.395	14.991 ± 0.035	0.737	2.919
130346	J014554.39+241555.0	0.035	-0.467	16.165 ± 0.056	1.107	4.098
130679	J015446.09+014326.0	0.039	0.208	16.544 ± 0.074	0.813	3.485
170240	J023850.49+272159.0	0.005	0.062	14.688 ± 0.030	0.712	2.550
64260	J075824.77+202352.3	0.035	-0.631	16.317 ± 0.074	1.519	3.894
135305	J083538.40-011407.0	0.044	0.812	12.038 ± 0.006	1.015	3.515
10311	J084624.06+540915.9	0.031	0.434	15.606 ± 0.042	0.951	3.219
135720	J091108.59+541051.9	0.027	-0.596	15.816 ± 0.042	0.768	3.852
135754	J091305.00+284845.0	0.027	-0.285	16.998 ± 0.119	1.079	4.042
136250	J095643.10-030409.0	0.047	0.700	14.258 ± 0.028	0.670	2.857
138274	J105301.99+365811.9	0.026	-0.268	16.522 ± 0.077	0.852	3.956
141379	J122655.39+424208.0	0.009	1.058	14.945 ± 0.032	0.858	4.197
171667	J123948.06-171753.9	0.028	0.788	13.990 ± 0.026	0.867	4.112
142435	J125037.90+434519.9	0.039	0.418	15.316 ± 0.036	1.464	3.222
142555	J125615.79-032723.0	0.045	0.146	16.044 ± 0.054	0.773	3.421
143373	J132119.70+320824.9	0.018	-0.019	16.823 ± 0.088	1.068	3.845
144502	J140609.20-032224.0	0.055	0.267	15.951 ± 0.050	0.917	3.547
53934 <sup>d</sup>	J155320.20+420735.6	0.022	0.443	15.757 ± 0.037	1.092	3.097
171765	J204609.92-160058.2	0.033	0.240	14.964 ± 0.037	1.123	3.162
44938 <sup>d</sup>	J211012.75+002428.2	0.020	0.638	16.368 ± 0.076	1.446	3.154
150295	J225515.30+180835.0	0.043	-0.192	13.158 ± 0.025	1.368	3.947
150927	J231544.60+065439.0	0.008	0.043	12.430 ± 0.007	0.791	3.704
152731	J235005.99+163505.9	0.049	-0.575	16.725 ± 0.099	1.062	3.601

<sup>a</sup> Objects from Reines et al. (2013). The SDSS and *WISE* thumbnails for these objects are shown in Figure 2.

<sup>b</sup> The SDSS and *WISE* thumbnails for these objects are shown in Figure 8.

<sup>c</sup> The SDSS and *WISE* thumbnails for these objects are shown in Figure 10, 11, and 12 in the Appendix.

<sup>d</sup> These objects have SDSS spectra, but one or more of the the emission lines used for BPT selection lack sufficient S/N for our optical classification.

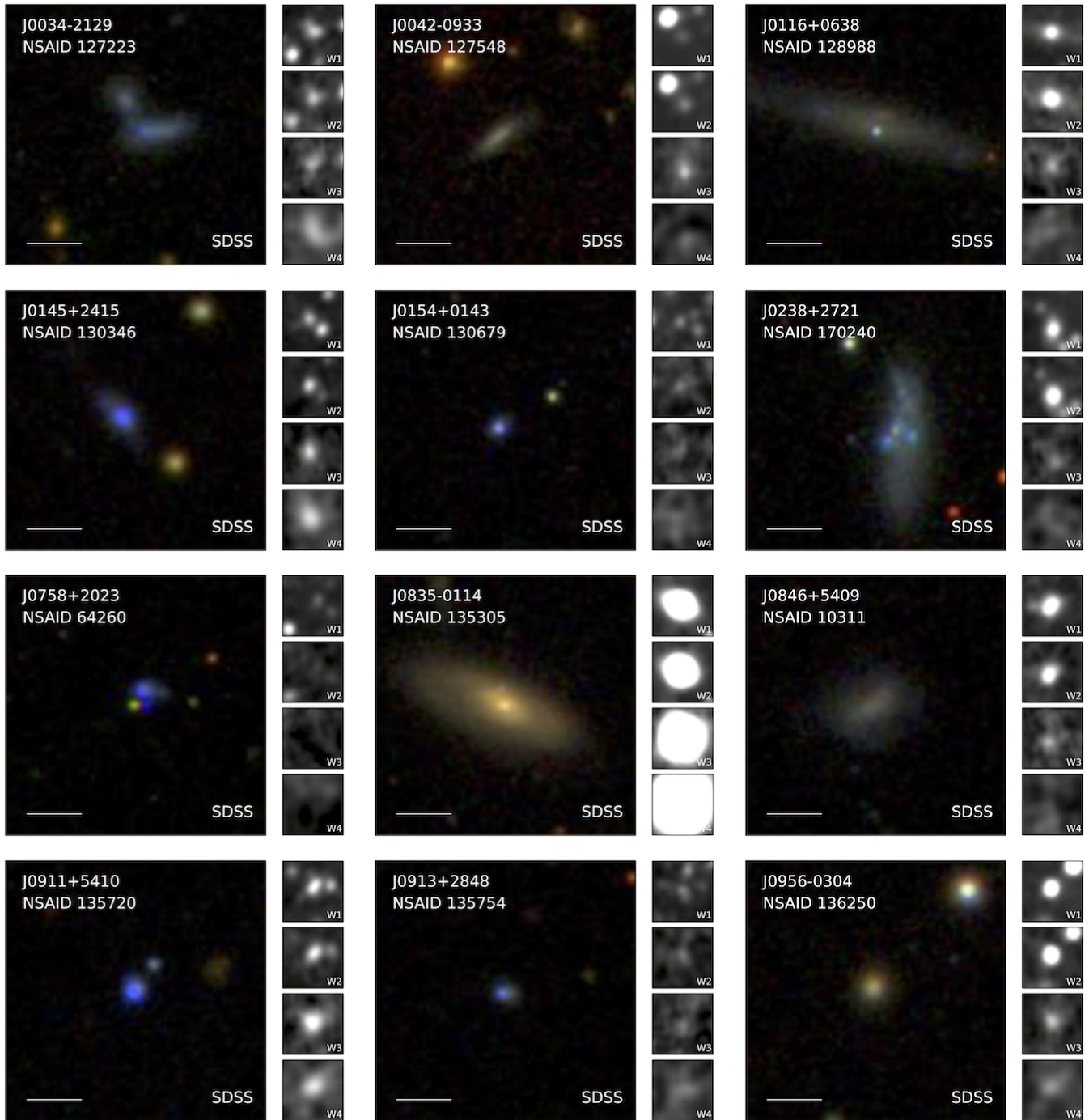


FIG. 10.— SDSS and *WISE* thumbnails for the Jarrett et al. *WISE* AGN candidates without optical emission line flux measurements. Each object is labelled as in Figure 8.

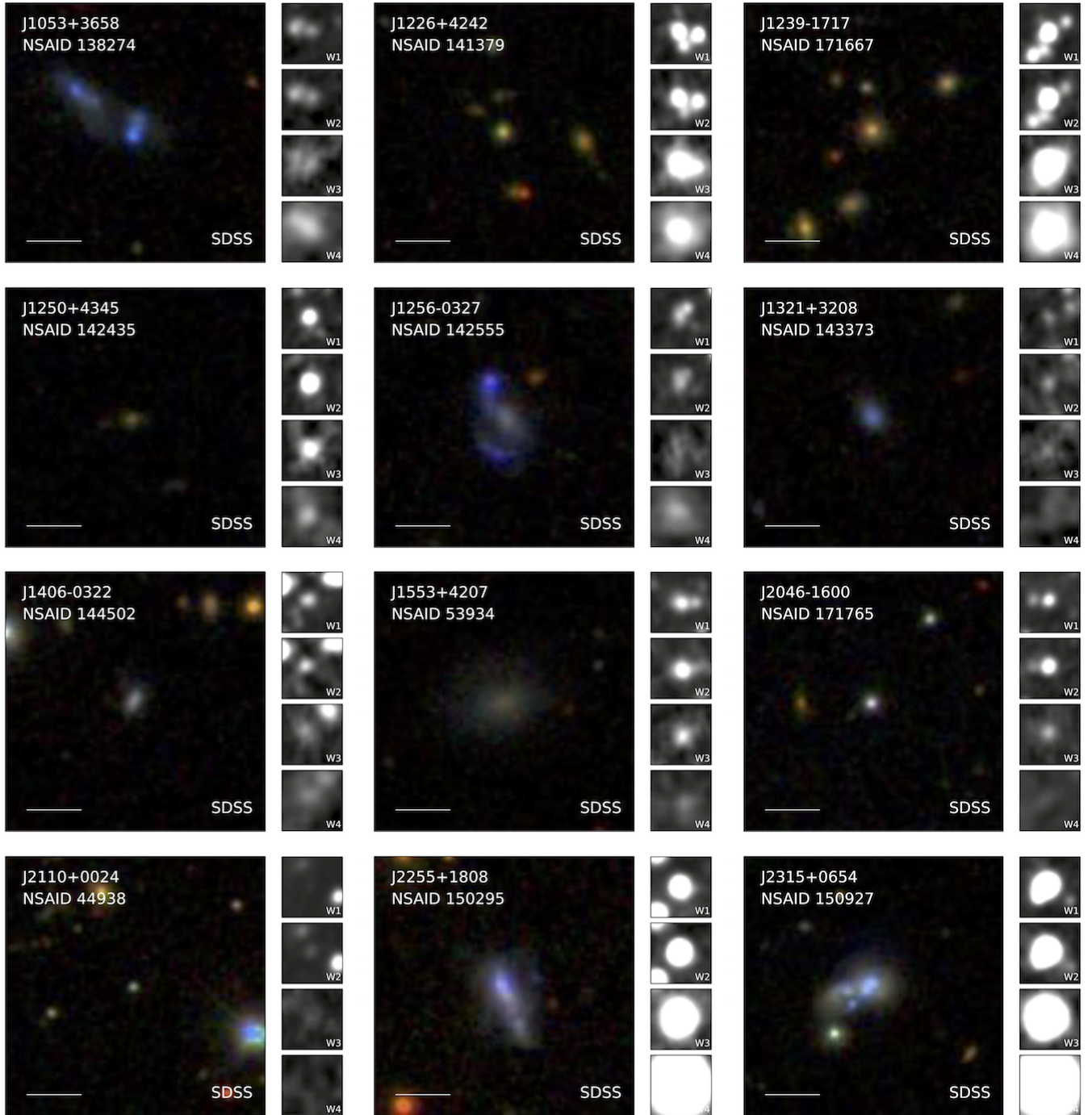


FIG. 11.— (Continued from Figure 10) SDSS and *WISE* thumbnails for the Jarrett et al. *WISE* AGN candidates without optical emission line flux measurements. Each object is labelled as in Figure 8.



FIG. 12.— (Continued from Figure 10) SDSS and *WISE* thumbnails for the Jarrett et al. *WISE* AGN candidates without optical emission line flux measurements. Each object is labelled as in Figure 8.